The relative importance of wind-driven and chimney effect cave ventilation: Observations in Postojna Cave (Slovenia)

Lovel Kukuljan[a], Franci Gabrovšek[a,*], Matthew D. Covington[b]

[a] Karst Research Institute ZRC SAZU, Titov trg 2, 6230 Postojna, Slovenia. E-mail: lovel.kukuljan@zrc-sazu.si; gabrovsek@zrc-sazu.si. https://orcid.org/0000-0001-5321-8335 (LK), https://orcid.org/0000-0001-8397-6487 (FG)

[b] Department of Geosciences, University of Arkansas, Fayetteville, AR 72701, Arkansas, USA. E-mail: mcoving@uark.edu. https://orcid.org/0000-0003-4044-7387

*Corresponding author: Franci Gabrovšek, Karst Research Institute ZRC SAZU, Titov trg 2, 6230 Postojna, Slovenia. E-mail: gabrovsek@zrc-sazu.si

19 **Abstract**

20   Density-driven chimney effect airflow is the most common form of cave ventilation, allowing

21   gas exchange between the outside and the karst subsurface. However, cave ventilation can

22   also be driven by other mechanisms, namely winds. We discuss the mechanism and dynamics

23   of wind-driven ventilation using observations in Postojna Cave, Slovenia. We show how

24   seasonal airflow patterns driven by the chimney effect are substantially modified by outside

25   winds. Wind flow over irregular topography forms near-surface air pressure variations and thus

26   pressure differences between cave entrances at different locations. These pressure

27   differences depend on wind speed and direction and their relationship to surface topography

28   and the location of cave entrances. Winds can act in the same or opposite direction as the

29   chimney effect and can either enhance, diminish or even reverse the direction of the density-

30   driven airflows. To examine the possibility of wind-driven flow, we used a computational fluid

31   dynamics model to calculate the wind pressure field over Postojna Cave and the pressure

32   differences between selected points for different configurations of wind speed and direction.

33   We compared these values with those obtained from airflow measurements in the cave and

34   from simple theoretical considerations. Despite the simplicity of the approach and the

35   complexity of the cave system, the comparisons showed satisfactory agreement. This allowed

36   a more general assessment of the relative importance of wind pressure for the subsurface

37   ventilation. We are certain that this example is not unique and that the wind-driven effect needs

38   to be considered elsewhere to provide better insights into the dynamics of cave climate, air

39   composition or dripwater geochemistry.

40   **Keywords:** cave airflow, pressure difference, driving mechanism, microclimate, Postojna

41   Cave

42   **Highlights:**

43   ● Winds can enhance or diminish typical seasonal density-driven cave ventilation

44   ● The wind-driven effect is generated by variations in the wind pressure field

45   ● The effect depends on the cave configuration and its surface connections

46   ● This study provides a better understanding of cave climate and karst processes

47

48   **INTRODUCTION**

49   Advection is the main driver of spatial and temporal variations in atmospheric parameters in the

50   karst vadose zone. Subsurface airflows are controlled by cave geometry, its connection with the

51   surface, and variations in external weather and climate (Cigna, 1968; Badino, 2010; Borsato et al.,

52   2015; James et al., 2015). In karst areas with temperate climates and adequate topographic

53   variation, the most common driving force is the density difference between outside and cave air.

54   The inside and outside air temperatures, and thus densities, often differ, resulting in pressure

55   differences that drive airflow between entrances at different elevations. In the warm period, the

56   internal air is heavier and the airflow is directed from higher to lower entrances. In the cold periods,

57   the situation is reversed. The typical term for density- or buoyancy-driven airflow is the "chimney"

58   or "stack effect" (Covington & Perne, 2015).

59   Other sources of ventilation in caves are possible. In caves with large cavities and small

60   connecting passages or entrances, pressure equalization with outside barometric changes results in

61   measurable barometric airflow within the passages (Conn, 1966; Pflitsch et al., 2010). Outside

62   wind flow over surface relief causes near-ground pressure variations and thus possible pressure

63   differences between different entrances of cave systems. The mechanisms of natural ventilation,

64   both density- and wind-driven, are well known to architects and civil engineers (Allard & Ghiaus,

65   2006; Yang & Clements-Croome, 2012). However, wind-driven or wind-induced ventilation in

66   caves has only been explored in a handful of studies (Kowalczk & Froelich, 2010; Fairchild &

67   Baker, 2012; Noronha et al., 2017; Riechelmann et al., 2019; Kašing & Lenart, 2020; Mattey et al.,

68   2021). In some environments, such a ventilation mechanism may dominate over the chimney effect.

69   For example, in a single-entrance cave in a tropical environment, where seasonal airflows are not

70   expected, Noronha et al. (2017) showed that trade winds cause a seasonal decrease in cave air pCO_2

71   and a concomitant increase in calcite precipitation. One may wonder about the significance of such

72   effects on cave climate, air composition, and carbonate chemistry for other caves and karst areas

73   in general.

74   In this study we investigate the influence of winds on the ventilation pattern of Postojna Cave,

75   Slovenia, and compare the observations with theoretical estimates and estimates obtained from a

76   topographic wind flow model. These results build on our previous findings of the strong influence

77   of outside winds on the seasonal cave ventilation (Kukuljan et al., 2021). The procedures discussed

78   here can be applied in any other karst area where there are sufficient winds and where the

79   configuration of the cave and its entrances allow for detection of the wind-driven effect.

80   <div align="center">**THEORETICAL AIRFLOW DRIVING PRESSURES**</div>

81   We can safely assume that the airflows measured in karst conduits are turbulent. In this case, the

82   relationship between airflow velocity and pressure difference can be approximated by one of the

83   empirical relations for turbulent flow in a pipe such as the Darcy-Weisbach Equation, which yields

84   a square-root relationship between the airflow velocity and the driving pressure $v \propto \sqrt{\Delta p}$. In the

85   simplest scenario of a cave with two entrances with a relative height difference of Δh, an outside

86   temperature of T_{out} and a cave air temperature of T_{in}, one can approximate the driving pressure,

87   Δp_c, as the difference between the hydrostatic pressures of the air columns outside and inside the

88   cave, $\Delta p_c = (\rho_{out} - \rho_{in})g\Delta h$. Written in a more explicit form as a function of temperature, this

89   gives:

90
$$\Delta p_c = \frac{p_0 M (T_{in} - T_{out})}{R T_{in} T_{out}} g \Delta h \qquad\qquad (1)$$

91   where ρ_{out} is the density of the outside air, ρ_{in} is density of the inside air, g is the gravitational

92   acceleration, p_0 is the atmospheric pressure at the lower entrance, M is the molar mass of dry air,

93   and R is the gas constant. This relationship assumes that the atmosphere is an isothermal

94   incompressible ideal gas, which is appropriate for small height differences. In this notation, the

95   sign of Δp_c is positive in cold periods ($T_{in} > T_{out}$) and negative in warm periods ($T_{in} < T_{out}$). For

96   temperature $|\Delta T| = |T_{in} - T_{out}| = 20°C$, $T_{in} = 10°C$, and standard pressure $p_0 = 101.325$ kPa, this

97   approximation gives a driving pressure of about 0.9 Pa/m, which corresponds to about 90 Pa for an

98   altitude difference of 100 m (Fig. 1).
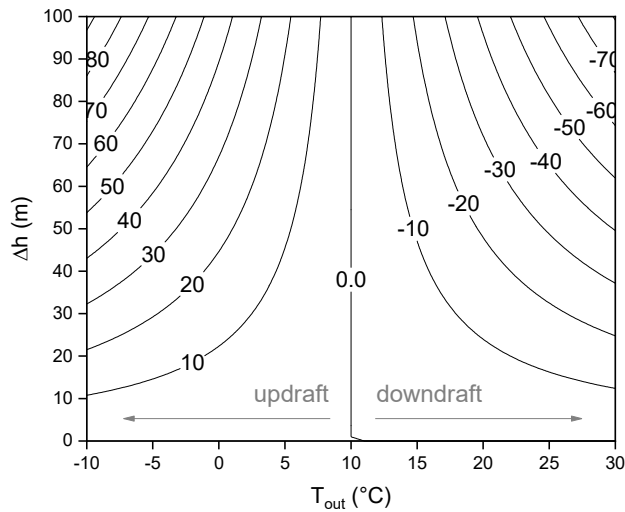
Fig. 1. Hydrostatic pressure variation as a function of outside temperature and altitude difference at p_0 = 101.325 kPa and T_{in} = 10°C. A positive Δp_c causes an upward airflow (updraft) in the system (air exits out from the upper entrance), while negative values cause a downward airflow (downdraft; air exits at the lower entrance).

Such small differences in pressure are difficult to measure directly, since the accuracy of barometers is usually in the range of a few hundred Pascals. Both airflow velocity and air temperature difference are routinely measured in caves and should display an approximately square-root relationship, $v \propto \sqrt{|\Delta T|}$, if ventilation is driven primarily by the chimney effect (Luetscher et al., 2008; Badino & Chignola, 2019; Covington et al., 2021). Many causes, such as frictional pressure losses, heat exchange, or rapidly changing conditions, are excluded from this relationship, but as a rule of thumb the relation is justifiable.

The near-surface pressure variations caused by wind flow over the topography are not easy to estimate. They depend on local wind speed and direction, terrain morphology, and surface roughness. The drag and lift effects caused by the dynamic pressures of the wind generally increase with the square of wind speed, which is a consequence of Bernoulli's equation. In general, the wind or velocity pressure, p_w, has the form,

$$p_w = \frac{1}{2} C_p \rho_{out} v_w^2 \, , \tag{2}$$

116   where C_p is a dimensionless coefficient containing the complexities associated with surface

117   roughness, topography, and general flow pattern, and v_w is the wind velocity. For simple cases, C_p

118   can be obtained from empirical calculations, while for more complex scenarios, computational

119   fluid dynamics (CFD) simulations are commonly used (Zheng et al., 2018). Basically, the wind

120   will induce a positive pressure on the windward side (a positive sign in C_p) and a negative pressure

121   on the leeward side (a negative sign in C_p). The value of C_p is usually between –1 and 1 (Zheng et

122   al., 2018).

123   If a cave extends between two entrances (E_1 and E_2), the driving pressure Δp_w induced by the

124   outside wind is equal to the difference of wind-induced pressures measured at the two entrances.

125   For this, we used the following notation: $\Delta p_w = p_w^{E1} - p_w^{E2}$. Therefore, Δp_w will have positive

126   values when entrance E_1 is facing the wind and negative values when entrance E_2 is facing the

127   wind. Considering the same standard pressure p_0 and temperature range (–10°C to 30°C) as in the

128   chimney flow estimation, a wind velocity v_w reaching up to 15 m/s, and a conservative C_p value of

129   0.5 (windward side in an open area), the wind pressures reach ~5.0±0.4 Pa at $v_w = 4$ m/s and ~70±5

130   Pa at $v_w = 15$ m/s. Considering the cave airflow driven solely by the wind effect, since $v \propto \sqrt{|\Delta p_w|}$,

131   the relationship between cave airflow velocity and external wind speed should be linear for wind

132   in a given direction according.

133   The similar magnitude of the pressure difference estimates of both driving mechanisms indicates

134   that both mechanisms could be important, but their exact values remain speculative and uncertain

135   due to the large number of unknowns and the high variation of wind speed and direction. We can

136   assume that the total pressure difference between the cave entrances is equal to the contribution of

137   both density- and wind-driven pressures, which leads us to $v \propto \sqrt{|\Delta p_c + \Delta p_w|}$. Depending on the

138   sign, the pressure differences generated by wind and the chimney effect may cancel each other out

139   and reduce ventilation, or they may reinforce each other. Theoretically, this can be illustrated as

140   four end cases, which are shown in Fig. 2.

141
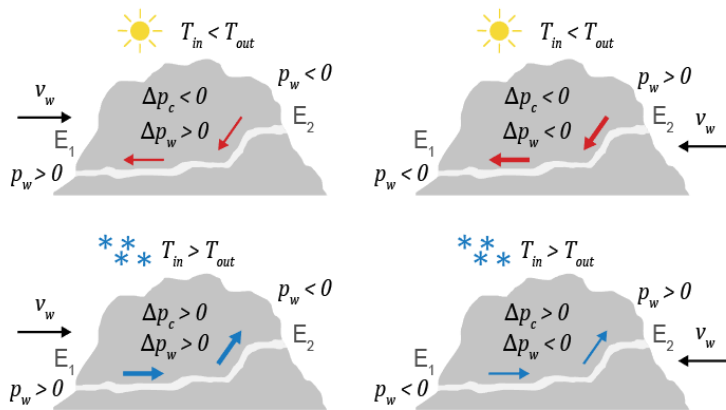
Fig. 2. Schematic representation of a cave within a karst massif under the influence of both density- and wind-driven ventilation. The two upper cases show a typical downdraft during a warm period conveying the air from the upper entrance, E_2, toward the lower entrance, E_1, (red arrows). In the upper left case, E_1 is faced toward the wind, thus resulting in a lower total pressure difference Δp between entrances. In the upper right case, the entrance E_2 is faced by the wind, which enhances the airflow driving force. The opposite occurs during the cooler period (two lower cases) when updraft dominates (blue arrows).

STUDY SITE

Postojna Cave is a cave system with multiple entrances near Postojna, Slovenia (Fig. 3a), known primarily as a tourist attraction with a centuries-long history of tourism, an underground railway, and extensive passages richly decorated with speleothems (Šebela, 2019). The system extends over two dominant levels. The lower epiphreatic level is characterized by a perennial flow of the Pivka River, which sinks into the cave at the boundary between the Pivka Basin and the karst plateau (Fig. 3a). The upper level is a complex network of passages and breakdown chambers rich in speleothems and fluvial cave sediments. There are five known entrances to the system. The lowest main entrance (ME) is located on the south-facing escarpment about 20 m above the ponor. There are probably a number of other smaller and inaccessible openings that connect the cave network to the surface 30 to 100 m above (Šebela, 2010). This results in efficient ventilation throughout the year. In the cooler months, the cave is ventilated by upward air circulation (updraft), while in the warmer months downward air circulation (downdraft) prevails (Šebela & Turk, 2011).

The easternmost side passages in Postojna Cave are Pisani Passage and Brezimeni Passage (Fig. 3c). Although they are of similar length (~500 m) and both terminate by breakdown or flowstone choke, their microclimatic characteristics are quite different. The Brezimeni Passage (BP) has a

163 large variation in air temperature (~2°C) and low, near-atmospheric $p\mathrm{CO_2}$ values, regardless of the

164 ventilation regime, indicating a strong connection with the surface (Kukuljan et al., 2021). Pisani

165 Passage (PP), on the other hand, is most likely connected to the surface by a dense network of

166 narrow airflow pathways that efficiently damp air temperature variations and form a strong source

167 of $\mathrm{CO_2}$ during warm periods (Gregorič et al., 2013; Prelovšek et al., 2018).

168   The region surrounding the cave system contains mountain ranges of the Dinaric Alps, among

169 which some peaks reach 1000 m a.s.l. (Fig. 3a). The lowland between the mountains is a forested

170 karst terrain densely populated with dolines of various sizes and origins (Fig. 4). Small solution

171 dolines predominate, but large collapse dolines are important features, as their deepest points

172 almost reach the level of active underground water flow. The ponor of the Pivka River is at 529 m

173 a.s.l., while the water channels gradually descend towards the resurgence at Planina Cave to 453

174 m a.s.l. At the surface, above the central part of the system where most of the entrances are located,

175 the terrain rises to a maximum of 633 m a.s.l., or about 100 m above the lowest, Main entrance.

176 Postojna has a combination of subcontinental and sub-Mediterranean climate (Kozjek et al., 2017).

177 The coldest month is January with an average temperature of –0.1°C and the warmest is July with

178 19°C (1981–2010) (ARSO, 2021). The average annual precipitation is 1500 mm.

179   The two main regional winds in SW Slovenia are the Bora and Jugo. Bora is a generally cold

180 catabatic wind blowing from the north-northeast (NNE) towards the Adriatic coast (Rakovec et al.,

181 2009). The Bora is particularly known for its gustiness, where the average speed can be exceeded

182 by three times (Grisogono & Belušić, 2009). Strong Bora events typically occur in the colder

183 months, while the summer season is usually calmer. The Jugo is a southeasterly (SE) to

184 southwesterly (SW) wind that carries moist air from the Adriatic Sea. Speeds reach up to 15 m/s

185 offshore and it has a similar occurrence and duration to the Bora. The average annual wind speed

186 in Postojna is estimated at 3–4 m/s, while the surrounding ridges provide slightly higher values (4–

187 5 m/s) (Rakovec et al., 2009). Postojna is located at the foot of the orographic barrier and is

188 therefore largely under the influence of N and NE winds. This is further enhanced by the

189 topography, which channels air masses from inland (Fig. 4). A wind-rose diagram showing

190 representative wind conditions in the Postojna region is shown in Fig. 3b.
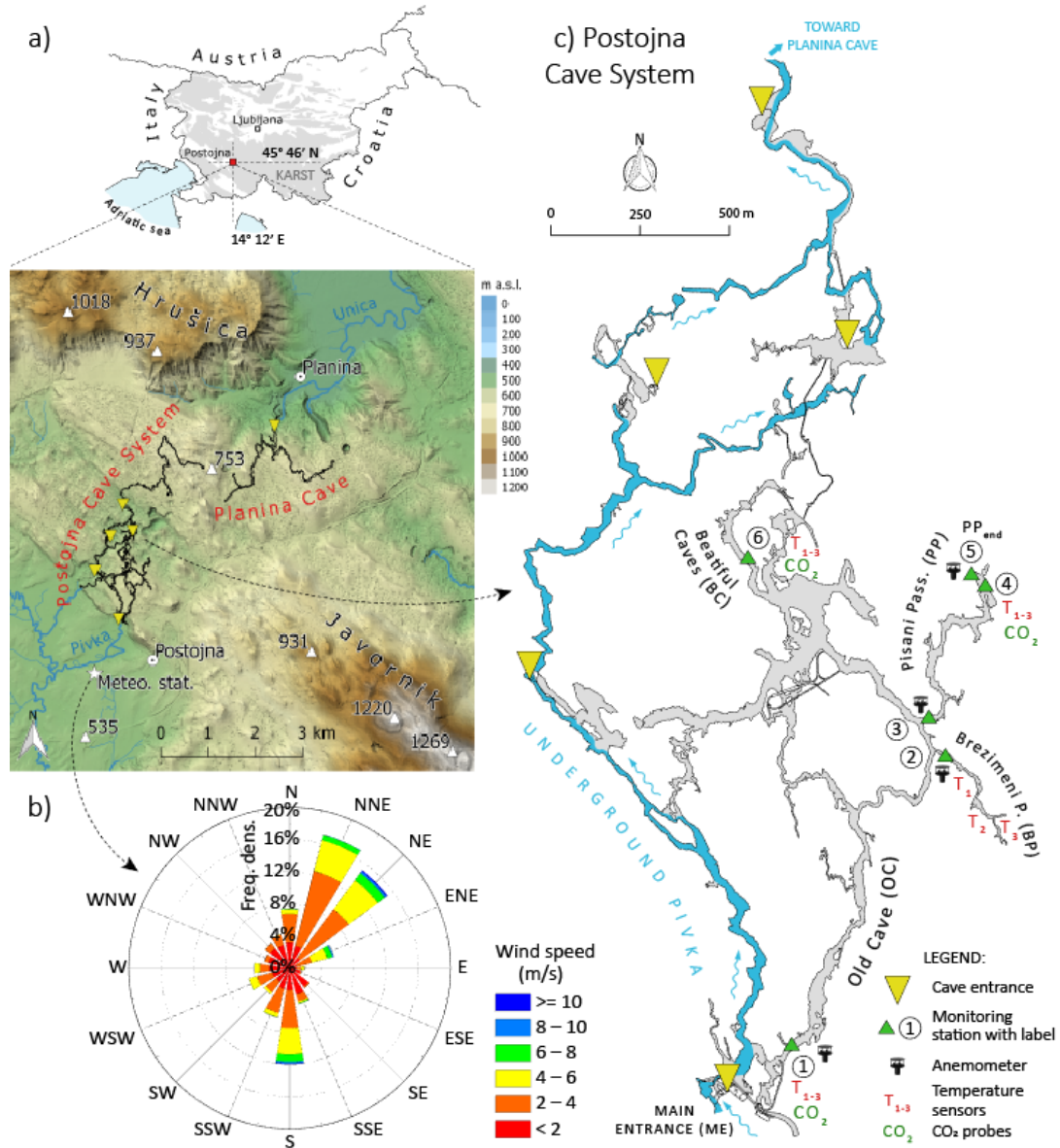
191

192 Fig. 3. (a) Geographic location and terrain map of the Postojna region between the Hrušica plateau and Javornik Hills. Black contour
193 lines show the extent of cave passages and yellow triangles are cave entrances. The location of the national meteorological station is
194 marked with a white star (S of Postojna Cave and W of Postojna). b) Wind-rose diagram of the national meteorological station with
195 wind speed, direction and frequency density for the period 2017–2020 grouped into 16 bins. (c) Map of Postojna Cave with continuous
196 climate monitoring sites (modified from Kukuljan et al. (2021)). Map source: cave cadastre at the ZRC SAZU Karst Research Institute.
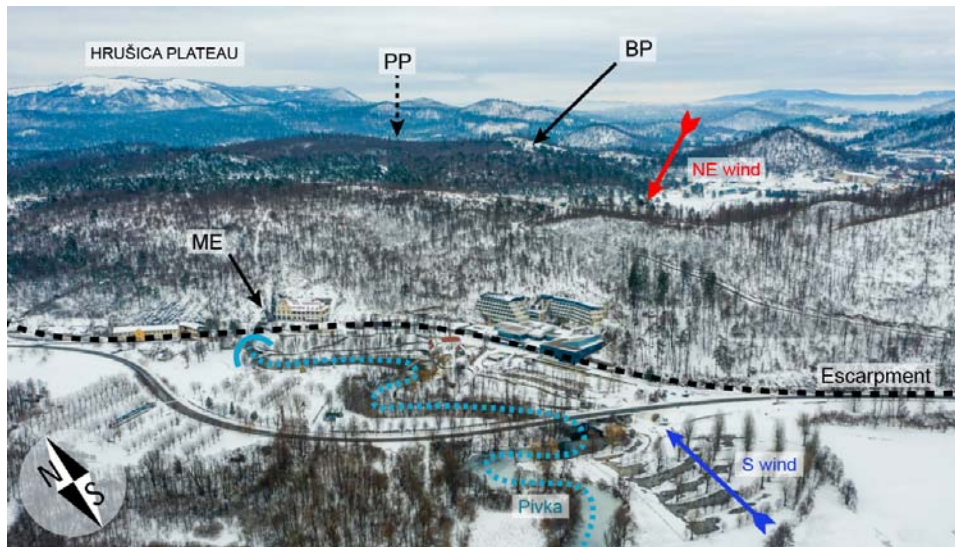
Fig. 4. Aerial view of the Main entrance (ME) of Postojna Cave and topography above the cave system showing the approximate positions of Pisani Passage (PP; behind the hill, not visible) and Brezimeni Passage (BP). The main wind directions are marked by red (NE) and blue (S) arrows. The escarpment is depicted with a black dashed line and the Pivka River with blue dashed line. The view is to the northeast. Geographic north is marked on the lower left.

MATERIALS AND METHODS

A still active cave monitoring network was established in 2009–2012 in Postojna Cave System, mainly to determine the microclimate and assess the potential impact of tourism on the cave environment (Fig. 3c) (Gabrovšek et al., 2014; Mlakar et al., 2020). The backbone of the network consists of four meteorological stations (Microstep CMS) with temperature, pCO_2 and airflow sensors. The stations are online, connected to a web server with data transmission via an optical cave line or via the Disruption Tolerant Network (DTN) protocol. A detailed description of the system and data management is available in Mlakar et al. (2020).

Station 1 was installed in a dominant airflow pathway near the main entrance to the cave (Old Cave, OC), stations 2–5 in remote, unvisited locations (BP and PP), and station 6 in the location where the influence of visitors is most expected (Beautiful Caves, BC). Stations 1, 3, 4, and 6 are connected to the web server via cable, while stations 2 and 5 record data by batteries. The stations record data at an interval of 1 s and record the statistics of the parameters with a resolution of 10 min: Ambient air temperature at three different heights with Pt100 sensors (stations 1, 4, and 6),

216 pCO_2 of the air (1, 4, and 6), and speed and direction of the airflow (1–4; Table 1). Ventilation

217 through PP is monitored at its entrance (site 3; PP_{ent}) and at its end (site 5; PP_{end}). At site 4, the

218 pCO_2 of the air is measured at two different heights, 6.5 m apart—one is near the floor, the other

219 at the ceiling. Ambient air temperature in BP was measured offline with data loggers at three sites

220 that have different microclimates.

221 Table 1. Summary of the equipment used in this study and its accuracy and measuring interval.

| Parameter	Equipment	Resolution (Accuracy)	Meas. interval	Comment
Airflow speed and direction	Gill Windsonic ultrasonic anemometer	0.1 m/s (±2% at 12 m/s) and 1° (±3° at 20 m/s)	10 min	Connected or battery powered
Air temperature	Pt100 sensor HOBO MX2203 TidbiT	0.01°C (±0.1°C) 0.01°C (±0.2°C)	10 min 10 min	Connected Battery powered
pCO_2	Vaisala GMP222 Vaisala GMP252	10 ppm (±2% of reading) 1 ppm (±2% of reading)	10 min 10 min	Range up to 10.000 ppm

222 Meteorological and climatic data of the outdoor conditions (air temperature and pressure, wind

223 speed and direction at 10 m) were obtained from the nearest national meteorological station 1.2 km

224 SSW from the main entrance of the cave (Fig. 3b) (ARSO, 2021). The sampling rate is 10 min and

225 the wind speed is available as an average value or as a maximum value (wind gust).

226 To evaluate Δp_w between different entrances of Postojna Cave, the Windstation CFD model was

227 used. The model simulates turbulent airflow over complex topography. It uses the control volume

228 approach to integrate the discretized Navier-Stokes, mass conservation and energy equations, and

229 a $k - \varepsilon$ turbulence model. The model accounts for forests and other obstacles by adding source

230 terms to the Navier-Stokes equation. The discretized equations are sub-relaxed and solved using

231 the SIMPLEC algorithm. Details of the model are beyond the scope of this article. An interested

232 reader can find more details on the algorithms and the use of the model in literature (Lopes, 2003).

233 The modelling was carried out by Menzio GmbH, the company responsible for the development

234 and licensing of the software. The topography was provided as a grid file representing a digital

235 elevation model (DEM) obtained from freely available LiDAR scans (ARSO, 2020). The 10 km ×

236 10 km modelling domain covers a wider region around Postojna and Postojna Cave (virtually the

237 entire area shown in Fig. 3b). The domain was discretized into cells with a planar dimension of 30

238 m × 30 m and 40 vertical layers, resulting in 4.8 million nodes. The region above the cave was

239 located in the central part of the modelling domain to minimize the influence of boundary

240 conditions. A zero gradient boundary condition was used for the downstream boundary. Closed

241 boundary conditions were used for the other three sides with no flow allowed to pass. The surface

242 roughness is important for the results. The spatial distribution of the surface roughness was

243 considered using a grid file with values of the aerodynamic roughness length z_0 over the entire

244 domain. The roughness length was estimated based on the satellite image of the area. The forest

245 model was active, with the forest height assumed to be a multiple of the roughness length. Given

246 the surface topography, roughness, and boundary conditions, the model computed a steady-state

247 solution for a given value of wind speed and direction at the meteorological station. We used 12

248 directions at 30° intervals with wind speeds ranging from 2–20 m/s in 2 m/s increments. A total of

249 120 simulations were performed.

250 **RESULTS AND DISCUSSION**

251 **Cave climate conditions**
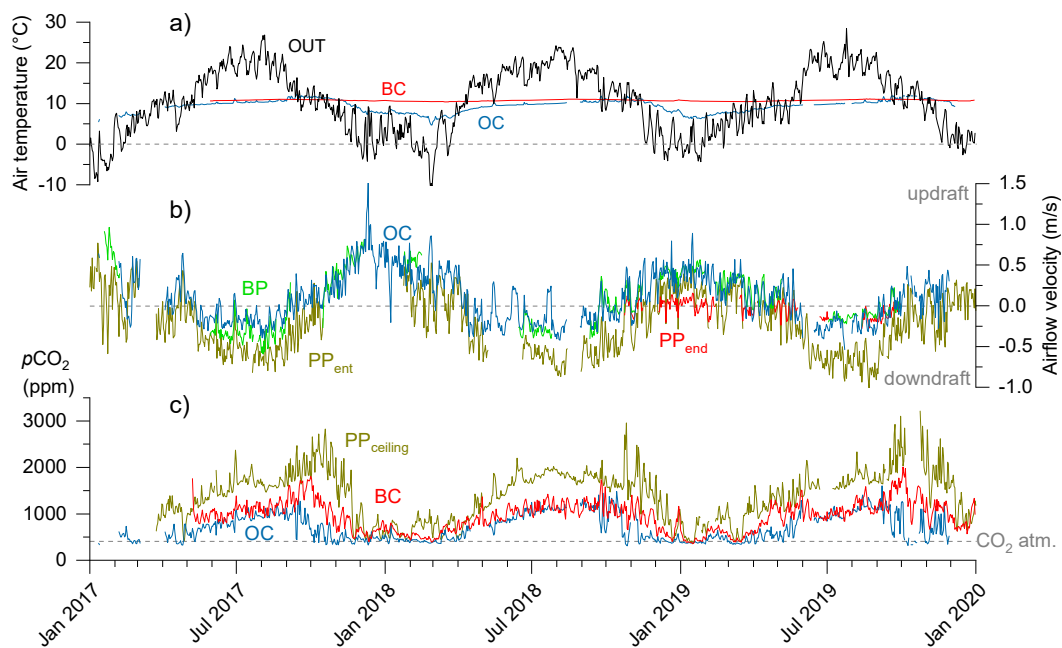
252

253 Fig. 5. Time series of Postojna Cave climate data for the entire study period (daily values): (a) temperature variation in the cave
254 compared to the outside temperature, (b) airflow velocities recorded in Pisani Passage, Brezimeni Passage and Old Cave with negative
255 values for a downdraft and positive values for an updraft, (c) pCO_2 time series recorded in Pisani Passage (ceiling), Beautiful Caves
256 and the Old Cave. The value of 410 ppm was taken as the atmospheric pCO_2 value (NOAA/ESRL, 2021).

12

257   Fig. 5 shows the typical seasonal pattern of microclimate parameters observed at all five climate

258   monitoring sites in Postojna Cave during the study period (2017–2020). Sites close to the main

259   airflow pathways, such as OC, were subject to a larger variation in air temperature (7°C) than the

260   inner parts of the cave, such as BC (0.8°C) or PP (0.1°C). Ambient air temperature measurements

261   showed irregularity in the cave, with PP being on average the coldest location (8.8°C), and BP the

262   warmest location (10.8°C). The airflow time series (Fig. 5b) distinguishes three different cave

263   ventilation regimes: Winter, summer and transitional. In cold periods, the cave air is lighter than

264   the outside air and flows upwards towards higher entrances and openings (updraft, positive sign),

265   while in warm periods the cave air is denser, flowing downwards and out of the lowest main

266   entrance (downdraft, negative sign). When the outside temperature is close to the cave temperature,

267   daily transitions between ventilation regimes can be observed. Because the air temperature in the

268   cave varies by a few degrees, the change in airflow direction does not occur simultaneously

269   throughout the cave. Moreover, while the seasonal variation is clearly visible, the airflow and pCO_2

270   signals have a distinctly jagged appearance that does not exactly follow the variation in ΔT. Such

271   behavior can occasionally occur even during periods when $|\Delta T|$ is >10°C, which would otherwise

272   cause strong chimney flow. In our previous study (Kukuljan et al., 2021), we suggested that these

273   brief interruptions, i.e., the temporary reversal of expected airflow directions, can be largely

274   attributed to the action of outside winds. As an example, Fig. 6 shows airflow velocities at PP_{ent}

275   for 2017–2020 plotted against the outside temperature. The original data set (red points) is widely

276   scattered. However, when windy periods are filtered out, a square-root relation between airflow

277   speed and T_{out} emerges. This is shown by green and blue points representing records when the

278   outside wind speed was below 3 m/s and 1 m/s, respectively.

13
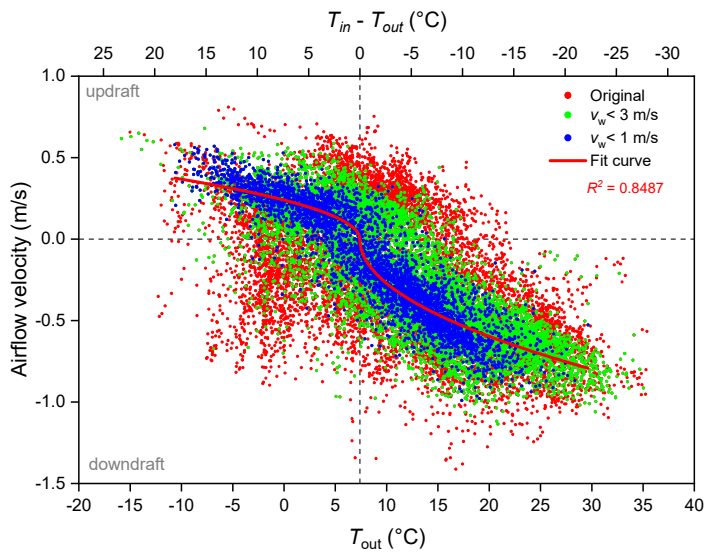
Fig. 6. Airflow velocity measured at PP$_{ent}$ plotted against outside temperature. Two filtering criteria were used: red points include all data points, green points those when $v_w < 3$ m/s, and blue points those when $v_w < 1$ m/s. The clearest chimney flow relationship and best square root fit ($R^2 = 0.8487$) is obtained when windy periods are excluded.

Wind characteristics

The wind-rose diagram in Fig. 3b shows that the three predominant wind directions in Postojna are north (N), north-northeast (NNE) and northeast (NE), representing the Bora wind, followed by south (S) and south-southwest (SSW), representing the Jugo wind. The distribution of these directions changes only slightly across seasons (Fig. 7a). The Bora (from now simplified as "NE wind") is active throughout the year, while the Jugo (from now "S wind") has a lower prevalence during the summer months and an overall lower prevalence during the year compared to the Bora. The distribution of wind speed also changes only slightly, but the average wind speed is generally higher in winter (3.1 m/s), than in summer (2.3 m/s). Fig. 7b shows the variations in wind speeds between two main wind sectors on a monthly basis. NE winds are generally the strongest throughout the year, with an average speed of 3.5 m/s, while S winds are weaker (average 2.6 m/s). The winds also show daily variation in speed and direction, but this variability has not been studied in detail.

14
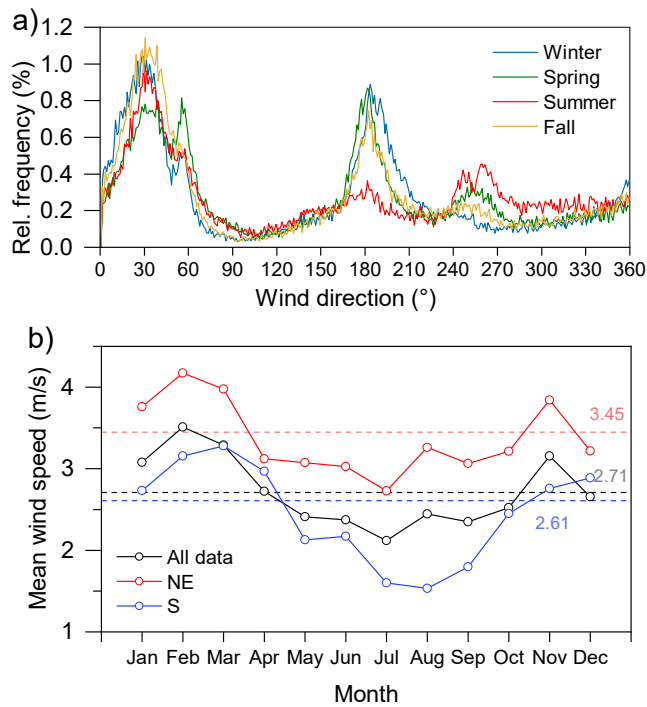
Fig. 7. a) Frequency distribution of wind direction for 2017–2020 grouped by season: Dec, Jan, and Feb (blue curve), Mar, Apr, and May (green curve,) Jun, Jul, and Aug (red curve), and Sept, Oct, and Nov (yellow curve). (b) Mean wind speeds for NE, S and all winds combined on a monthly basis. Dashed lines correspond to absolute means labelled with values.

Estimation of wind pressure field above Postojna Cave
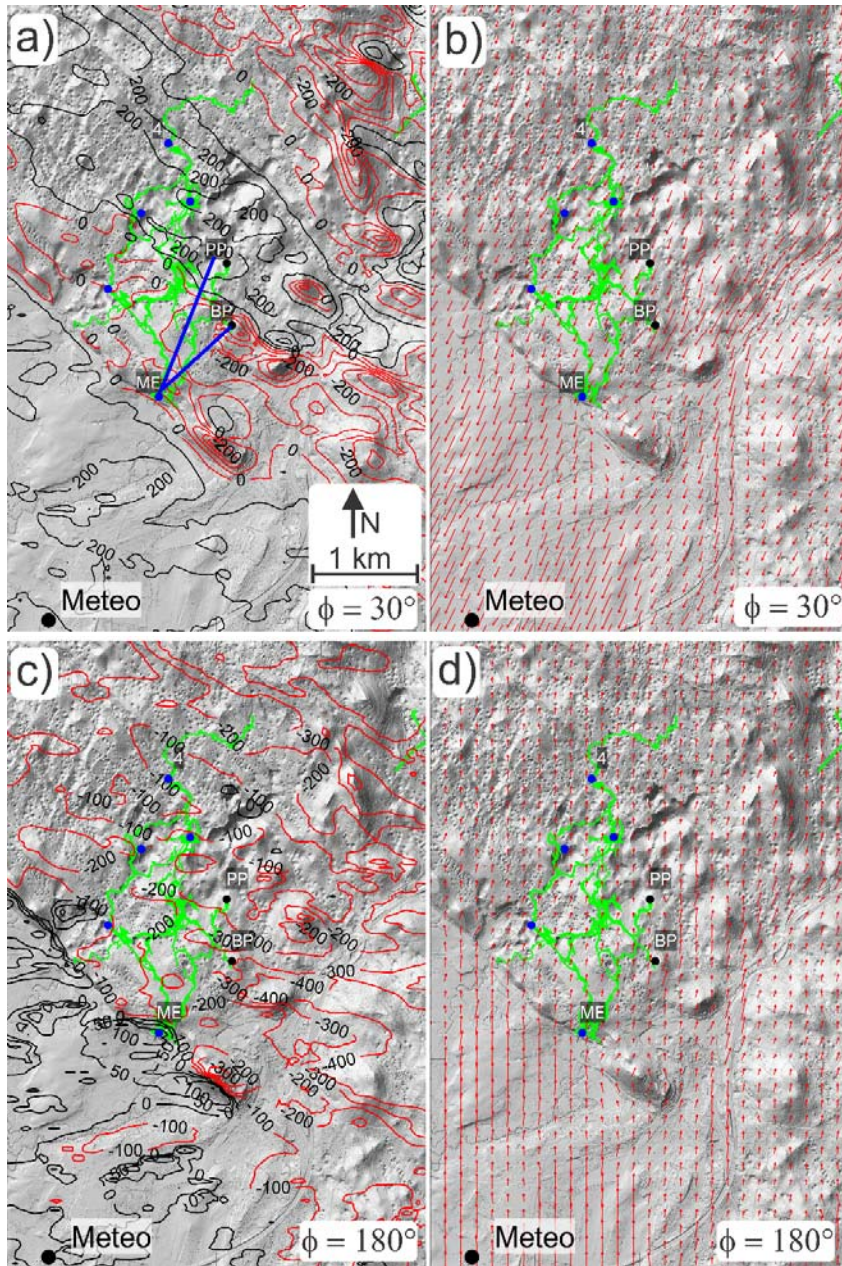
Fig. 8. Contour map of the wind pressure field in Pascals for different values at the meteorological station: (a) v_w = 10 m/s and ϕ = 30° and (c) v_w = 10 m/s and ϕ = 180°, and vector field map of wind velocity for: (b) v_w = 10 m/s and ϕ = 30° and (d) v_w = 10 m/s and ϕ = 180°. The green polygon marks the extent of the Postojna Cave passages. Black points and labels mark the positions of the meteorological station and terminal part of Pisani Passage (PP) and Brezimeni Passage (BP). The positions of the known cave entrances are marked by blue points, while the main entrance is also labelled (ME). The blue lines in (a) denote the profiles ME–PP and ME–BP.

16

308   Figure Fig. 8 shows the results of the Windstation model for the velocity and pressure field over Postojna

309   Cave System, when wind speed and direction at the meteorological station are $v_w = 10$ m/s and $\phi = 30°$

310   (NNE wind, Fig. 8a and b) or $v_w = 10$ m/s and $\phi = 180°$ (S wind, Fig. 8c and d). The model computes the

311   velocity pressure field relative to a reference point in the domain, where it is taken to be zero. Since we are

312   interested in pressure differences between selected points (e.g., location of cave entrances), this result is

313   sufficient. Note that when the wind speed is zero, the values of p_w in the entire domain are zero. In Fig. 8a

314   and c, the pressure field is uniformly shifted so that the zero value is in the region of the main entrance ME.

315   The black isobars are used for positive values and the red isobars for negative values; that is, black regions

316   have p_w greater than ME and red regions less. A brief review shows that Δp_w can reach several hundred

317   Pascals between different locations, which is comparable to or higher than the expected pressure differences

318   of the chimney effect. Airflow is diverted and/or channeled by topography, which also determines regions

319   with higher and lower wind pressures.

320   In NE winds, the depression near the terminal part of Pisani Passage (PP) has a higher pressure than the

321   region around the main entrance, while the region above the terminal part of Brezimeni Passage (BP) has a

322   negative pressure. The scarp between the Pivka Basin and the karst plateau plays a particularly important

323   role in S winds. Most of the area NE of the scarp where the cave system extends has a lower pressure than

324   the pressure around the main entrance.

325   To further illustrate the modelling results, we plot velocity/pressure profiles along two lines for different

326   wind speeds and directions in Fig. 9. The profiles, shown in Fig. 8a, connect the region above the terminal

327   parts of PP and BP and the Main entrance (ME–PP and ME–BP). Figure Fig. 9a shows the wind speed and

328   pressure 5 m above the ground along the line ME–PP for a wind direction of 30° (NNE) and for different

329   values of wind speed at the meteorological station (4, 6, 8 and 10 m/s). The grey shading represents the

330   topography along the profile. Δp_w between ME and PP increases approximately with the square of wind

331   speed. Figure Fig. 9b shows the same profile for the S wind ($\phi = 180°$), where the wind-driven effect drives

332   cave ventilation in the opposite direction with similar pressure differences between the ends of the profiles

333   as for the 30° case.

334   The wind pressure distribution was also estimated for other directions. Figure Fig. 9c shows the p_w along

335   the profile PP–ME for all directions in 30° steps at 5 m height and $v_w = 10$ m/s. The largest differences

336   between minimum and maximum p_w are found at 30° and 150°, and the smallest at 120° and 330° when the

17

337   winds blow parallel to the escarpment. The wind pressure in the profile ME–BP is shown in Fig. 9d for both

338     $\phi = 30°$ and $\phi = 180°$. Here, the wind pressure differences between ME and BP are smaller than at PP due

339   to the different topography. For both wind directions, Δp_w between the main entrance and the surface above

340   the BP is positive, with a higher pressure difference for S winds.

341
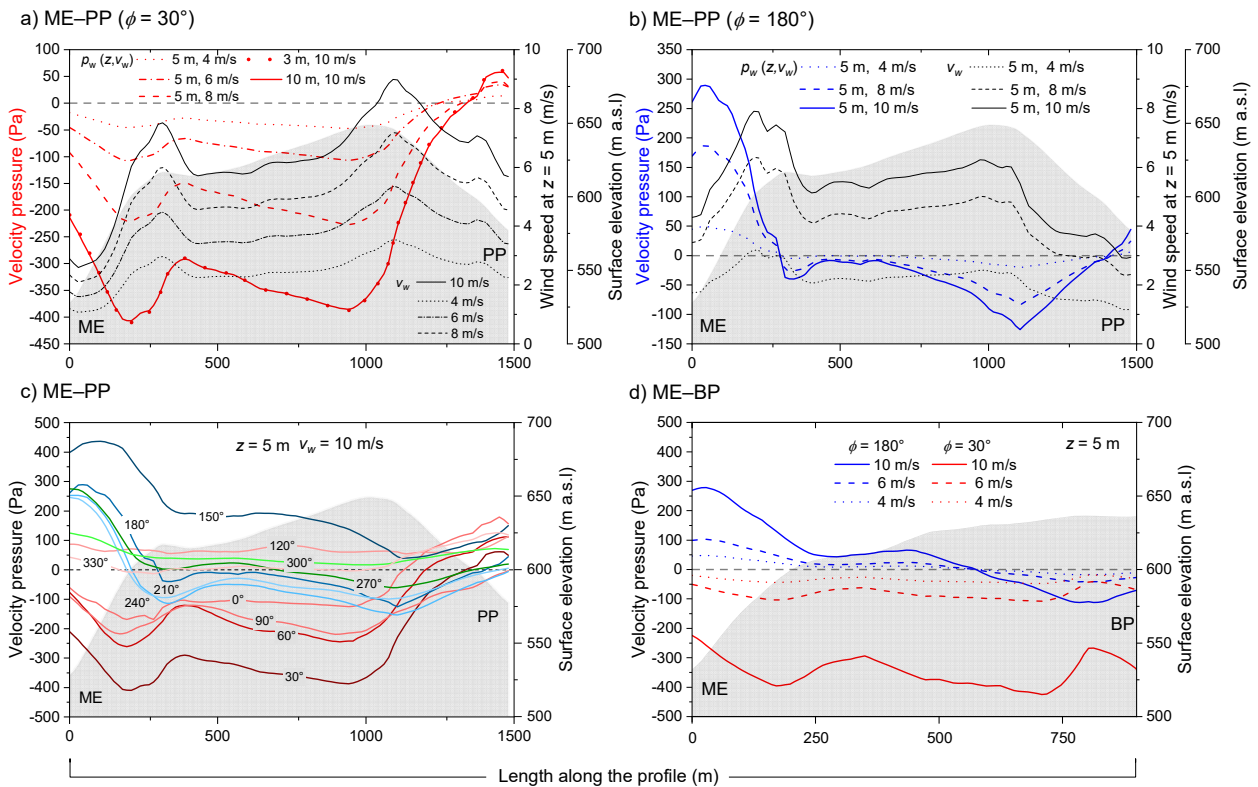
Fig. 9. Velocity pressure profiles along ME–PP with $\phi = 30°$ (a) and $\phi = 180°$ (b) for different wind speeds at the meteorological station (4–10 m/s). Velocity pressure profiles along ME–PP for all wind directions at 30° increments (c). d) Velocity pressure profile along ME–BP for $\phi = 30°$ and $\phi = 180°$ for different wind speeds at the meteorological station (4, 6 and 10 m/s).

345   The results of the CFD model, although quantitative, must be considered with some caution. The exact

346   numerical value of p_w is the result of several empirical assumptions that are incorporated in the model. We

347   have also neglected the fact that the pressure at the ground, where the entrances are located, is in fact not

348   calculated, since the wind profile is only valid for $z > z_0$. In addition, the domain discretization does not

349   allow us to account for small-scale surface irregularities, which certainly affect the local wind field.

18

Relationship between cave ventilation and wind

350
351   Seasonal variations in cave airflow direction indicate that the predominant mechanism of
352   ventilation in Postojna Cave is the chimney effect. Wind-driven pressure differences can either
353   increase or decrease the ventilation, and in extreme cases, even reverse its direction. To illustrate
354   this effect more clearly, we compared cave conditions (airflow and temperature) and outside
355   conditions (wind speed/direction and temperature) in shorter, 20-day windows. Fig. 10a shows a
356   cold period (when generally $T_{in} > T_{out}$), and Fig. 10b shows a warm period (when generally $T_{in} <$
357   T_{out}). For T_{in} we use the air temperature at PP (site 4), since this site has the most stable temperature
358   signal. To represent wind direction, we choose a convention where the outside wind velocity has a
359   positive sign for directions between 90° and 270° and a negative sign for directions above 270°
360   and below 90°. The wind time series has been colored according to the two most prominent
361   directions—NE winds are colored red, S winds are colored blue, while all others are colored gray.

362   In Fig. 10a, which represents a cold period, a dominant updraft driven by the chimney effect is
363   interrupted by short bursts of downdrafts. When the winds come from the NE, the airflow in the
364   cave will decrease or, if the wind is strong enough, it can cause a complete reversal of the cave
365   airflow direction (red arrows). Similarly, S winds will increase the updraft velocity (blue arrow).
366   In warm periods, the effect is the opposite (Fig. 10b). In a period dominated by downdraft, the NE
367   wind increases the airflow speed, while the S wind decreases it or even reverses it into an updraft.
368   In these two end-member cases, the value of $|\Delta T|$ can sometimes exceed 10°C, which would
369   typically cause a strong chimney effect. Despite this, however, for a short period of time, the cave
370   can ventilate in the opposite direction of the flow expected by the chimney effect. The onset,
371   duration, and termination of these events closely follow the wind events, and the effect can be
372   observed at each of the monitoring sites, albeit with varying intensity and pattern.
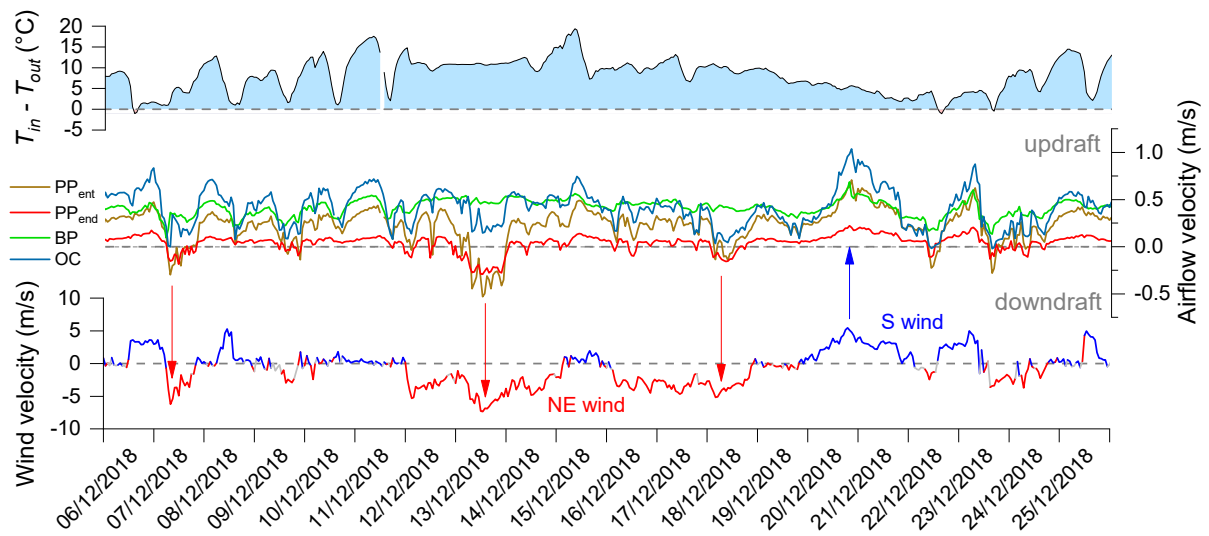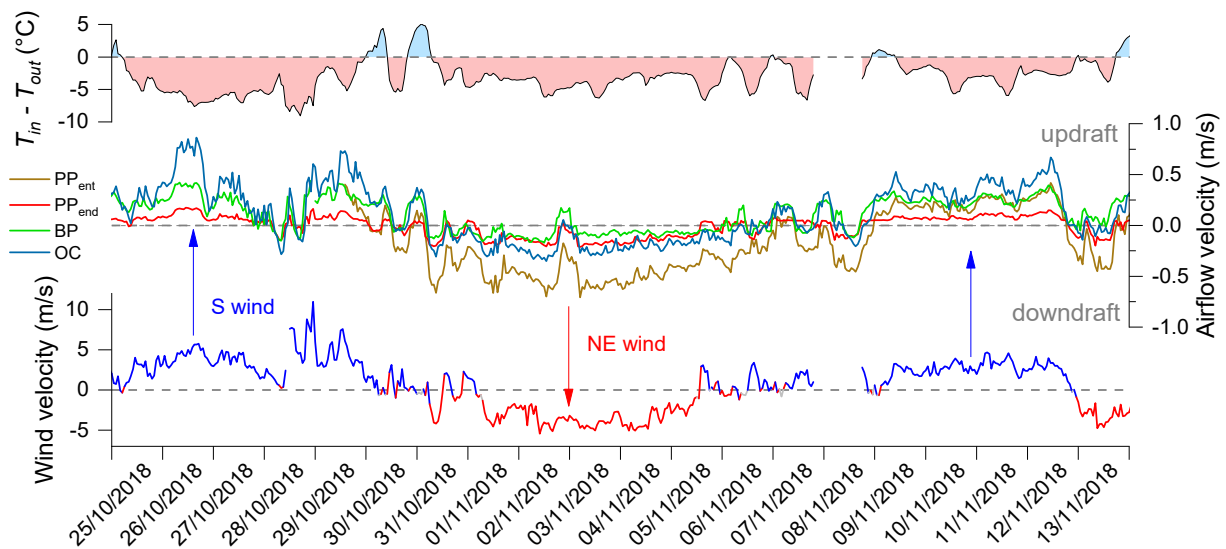
Fig. 10. Dynamics of airflow at Postojna Cave (center) as a function of temperature difference (top) and outside wind speed and direction (bottom) for the 20-day cold (a) and warm (b) periods. The airflow velocity time series (middle) are colored by location— PP_{ent} is yellow, PP_{end} is red, BP is green, and the OC is blue. Wind speed is colored as a function of direction—positive signs are given to all winds with directions from 90–270°, and negative for those coming from above 270° and below 90°. The time series are additionally colored by wind sector—winds from 330–90° are colored red, winds from 120–270° are colored blue, and all others are colored gray. Red arrows show the influence of the NE wind on the cave airflow, while the blue arrows represent the influence of the S wind.

381   The wind-driven effect is also evident when analyzing daily resolution data from the entire 2017–

382   2020 study period. In Fig. 11, airflow velocity has been plotted against outside temperature for the

383   most wind-prone site, PP_{ent}. Red points indicate the days with prevailing NE winds, while blue

384   points represent the days with prevailing S winds. These observations are consistent with the results

385   of the model presented in the previous chapter. The NE wind induces a negative Δp_w between the

386   lower and upper entrance, thus promoting a downdraft. On the other hand, S winds induces a higher

387   pressure at the lower entrance (ME) and therefore promote an updraft.
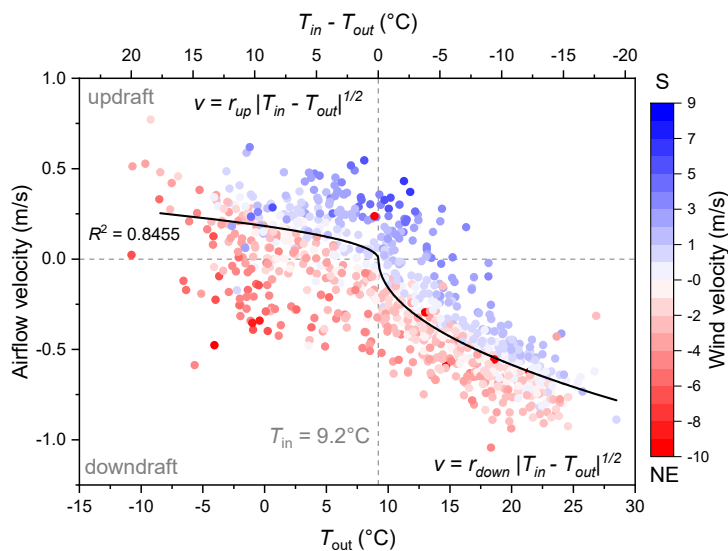
388

389   Fig. 11. The plot of daily average airflow velocity at PP_{ent} against outside temperature, color-coded by outside wind speed and direction.
390   The days with prevailing NE winds are colored red, while S winds are colored blue. Stronger color means stronger mean wind speed.
391   The square-root relationship (black curve) was fitted only with calm days (v_w < 2 m/s). The red and blue points are well separated,
392   indicating that wind direction has a consistent and predictable effect on cave airflow—NE winds enhance the downdraft, while S winds
393   enhance the updraft. The effect scales well with wind speed and shows greater scattering (deviation) from the theoretical relationship
394   on windy days.

395   **Spatial differences in the wind-driven effect**

396   The wind-driven effect is observed at all sites (Fig. 10a and b). However, the data show that the

397   effect varies from site to site. For example, OC and BP respond more strongly to S winds, while

398   sites in PP respond strongly regardless of wind direction. To best identify the wind-driven effect,

399   we filtered the hourly cave airflow velocity to select data when $T_{in} \approx T_{out}$ to minimize the

400   contribution of chimney effect. The filtered data are shown in Fig. 12 for three sites. In the case of

401   PP$_{ent}$, the outside temperature range of 8–10°C was taken as the filter criterion (about ±1°C from

402   the theoretical value in Fig. 11). A linear correlation was calculated separately for NE and S winds

403   (both at v_w > 1 m/s). The same procedure was repeated for OC (8°C < T_{out} < 10°C) and BP (10°C

404   < T_{out} < 12°C). For both BP and OC, a positive linear correlation is obtained only with updraft and

405   S winds, while NE winds showed weak or no correlation with cave airflow (Fig. 12).
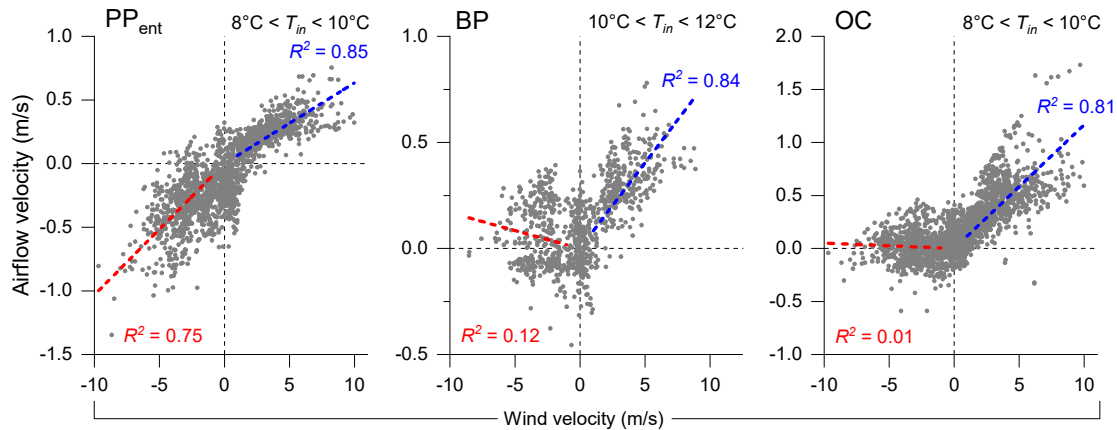
406

407   Fig. 12. Linear relationships between hourly wind velocities and airflow velocities (Pisani Passage (PP$_{ent}$), Brezimeni Passage (BP),
408   and Old Cave (OC)) at Postojna Cave in a bounded temperature range when $T_{in} \approx T_{out}$ is between 8–10°C (for PP$_{ent}$ and OC), and 10–
409   12°C (for BP). The linear regressions were calculated for wind speeds greater than 1 m/s.

410   Many factors may contribute to the spatial diversity of airflow patterns: the relative position of

411   the measurement site within the cave airflow pathway, its proximity to the nearest cave entrance,

412   the orientation and size of the entrance, and the position of the entrances within regional wind flows

413   and topography. The spatial differences discussed are in agreement with the results of the CFD

414   model. When comparing different topographic velocity pressure profiles, the model gives higher

415   pressure differences for the ME–BP profile than for the ME–PP profile for the S wind (Fig. 13).

416   When considering the effect of NE wind, the sign of the wind pressure depends on the profile—

417   along ME–PP a downdraft is forced, while along ME–BP an updraft is forced.

22
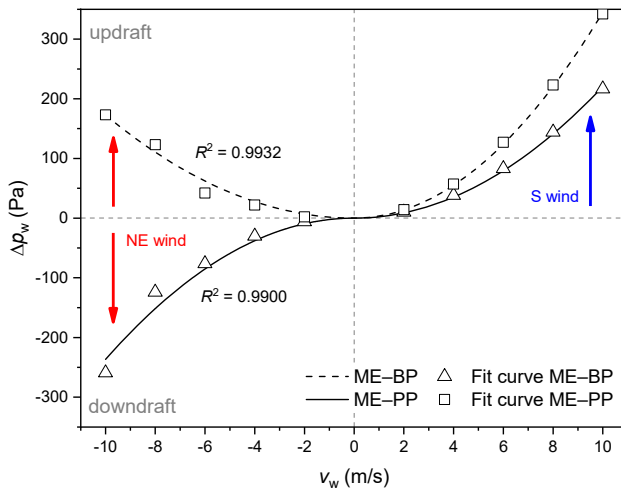
418

419 Fig. 13. Wind pressure differences between the Main entrance (ME) and Pisani Passage (PP; triangles) or Brezimeni Passage (BP;
420 squares) determined by the CFD model as a function of wind velocity. The points are fitted with a quadratic function, $\Delta p_w = c_w\, v_w^2$, and
421 the fit quality is quantified using R^2. S wind forces an updraft in both profiles, while NE wind forces an updraft in the ME–BP profile and
422 a downdraft in the ME–PP profile.

423   OC and BP show similar airflow characteristics. BP is found to be the main pathway connecting

424 the main entrance, OC and the surface (Fig. 4). The height difference between the passage and the

425 surface above is about 100 m in the case of BP and 40 m in the case of PP. Thus, the chimney effect

426 in BP is much stronger and the wind-driven effect is less pronounced than in PP. Moreover, the

427 airflow between BP and the surface is concentrated in a large vertical passage (chimney). High

428 temperature variations and low CO_2 content in the passage between the chimney and the connection

429 to OC during the downdraft indicate a good airflow connection to the surface (Kukuljan et al.,

430 2021). On the other hand, no dominant airflow pathway toward the surface was found in PP. These

431 differences are also reflected in the average volumetric flow rate—it is about 3.4 m³/s in BP

432 compared to 0.5 m³/s in PP.

433 **Scale and frequency of the wind-driven effect**

434   The CFD model produces the expected qualitative results, but the question remains how reliable

435 the quantitative predictions are. In this section, we compare the magnitude of the pressure

436 differences between PP and ME, derived from observations and calculated by the CFD model. The

437   model results are shown in Fig. 13 and Table 2, which give values of $\Delta p_w = p_w^{ME} - p_w^{PP}$ for wind

438   speeds between 2–10 m/s and directions $\phi = 30°$ and $\phi = 180°$ at a height of $z = 5$ m.

439   Table 2. Velocity pressure differences for the ME–PP profile for $\phi = 30°$ and $\phi = 180°$ according to the CFD model. These values are
440   plotted and fitted in Fig. 13.

	Δp_w (Pa)	
$|v_w|$ (m/s)	$\phi = 30°$	$\phi = 180°$
2	-6	10
4	-30	38
6	-76	83
8	-124	144
10	-259	216

441

442   To estimate the wind pressure difference from the data, we return to the theoretical considerations

443   from the first section. The airflow velocity has a square root dependence on the total pressure
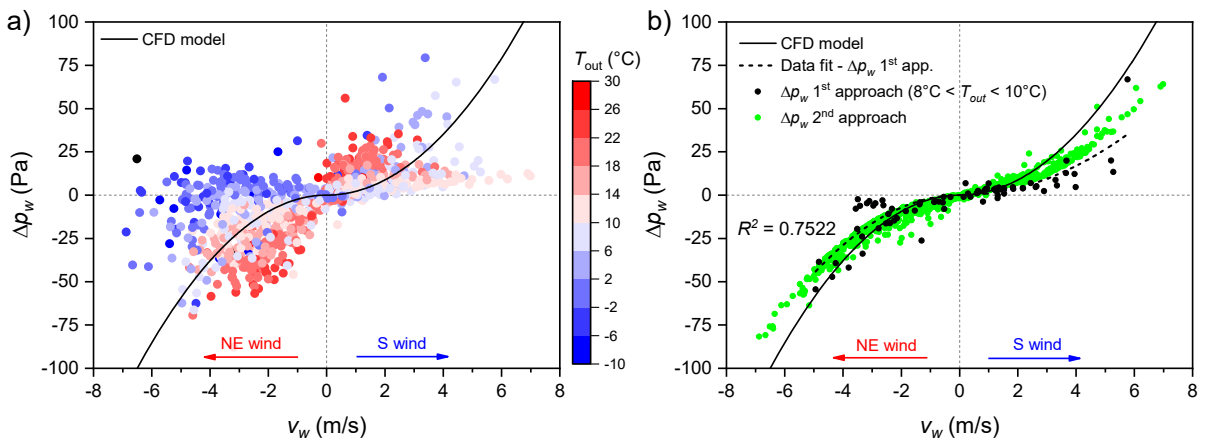
444   difference,

$$v = r\sqrt{|\Delta p_c + \Delta p_w|}. \tag{3}$$

446   Velocity is the only measured quantity in this equation, so to extract Δp_w we need an estimate for

447   r and Δp_c. The factor r, which depends primarily on the geometry of the airflow passages, can be

448   extracted from the data when the wind pressure is minimal, so that $v = r\sqrt{|\Delta p_c|}$ (Fig. 11; fitted

449   only on calm days only ($v_w < 2$ m/s)). Two resistance factors were determined separately for updraft

450   (r_{up}) and downdraft (r_{down}). The pressure difference of the chimney effect Δp_c is obtained from Eq.

451   1, using $\Delta h = 40$ m and $T_{in} = 9.2°C$ (the temperature that gave the best fit in Fig. 11 for Pisani

452   Passage and the T_{out} time series). We can now simply use Eq. 3. to calculate the remaining unknown

453   pressure difference using the measured airflow velocity:

$$\mp \Delta p_w = \left(\frac{v}{r}\right)^2 \pm \Delta p_c. \tag{4}$$

455   The sign of Δp_c and the choice of the resistance factor, r_{up} or r_{down}, depends on the airflow

456   direction, while the sign of Δp_w depends on the wind direction (S positive, NE negative). The results

457   presented in Fig. 14a show a very rough agreement between Δp_w of the CFD model and the value

24

458 estimated from the data. The scatter could be due to the uncertainties in the factor r resulting from

459 the fit with large scatter in the airflow velocity even for low outside winds (see Fig. 11). The origin

460 of the scatter is beyond the scope of this work. To address it, airflow in a much more complex

461 system than the one assumed here would have to be considered. To mitigate this scatter, we again

462 use only the points where $T_{in} \approx T_{out} = 9.2°C$, the situation where we expect the wind-driven effect

463 to be dominant (Fig. 14b). The quadratic curve fitted to these data (black points and black dashed

464 line) roughly follows the CFD model curve (solid line) with larger differences for stronger S winds

465 (>4 m/s).

466

467 Fig. 14. Comparison of the wind pressure differences, Δp_w, obtained with the two approaches discussed in the text. In (a), the data
468 points of the first approach are colored according to the outside temperature ranging from −10°C to 30°C as daily values, and the
469 points scatter around the model line with a predictable pattern due to the residual dependence on temperature. In (b), these points are
470 filtered by the 8°C < T_{out} < 10°C criterion (black points), fitted to a quadratic relationship (black dashed line; R^2 = 0.7522), and compared
471 with the results of the second approach (green points). Both results follow the theoretical quadratic relationship determined by the CFD
472 model (black curve).

473 Another way to estimate Δp_w is to consider situations where the airflow in the passage stops or is

474 close to zero. In this case the wind pressure is opposite to the chimney flow pressure, $\Delta p_w = -\Delta p_c$.

475 Thus, taking $\Delta p_w = c_w v_w^2$, and $\Delta p_c = c_c \Delta T$, where c_w and c_c are coefficients for the wind-driven

476 and chimney effects, we obtain a square-root relationship between wind velocity and temperature

477 difference, $v_w = \pm \sqrt{\left|\frac{c_c}{c_w}\right|} \sqrt{|\Delta T|}$ (Fig. 15). The goodness of fit, $R^2 = 0.5761$, gives some

478 justification to this approach. From Eq. 1. we obtain $c_c = \frac{\rho_{out} g \Delta h}{T_{in}}$. Here we have used an average

25

479   air density, ρ_{out} = 1.19 kg/m³, Δh = 40 m and T_{in} = 9.2°C, giving a c_c value of 1.65 K^{-1}. The

480   coefficient c_w is obtained from the fit between v_w and $\sqrt{|\Delta T|}$, separately for the effect of S (positive)

481   and NE wind (negative; Fig. 15). Finally, Δp_w is calculated from $\Delta p_w = c_w v_w^2$ and compared with

482   the first approach (Fig. 14b). Both approaches yielded similar estimates of Δp_w and show good

483   agreement with the CFD model.
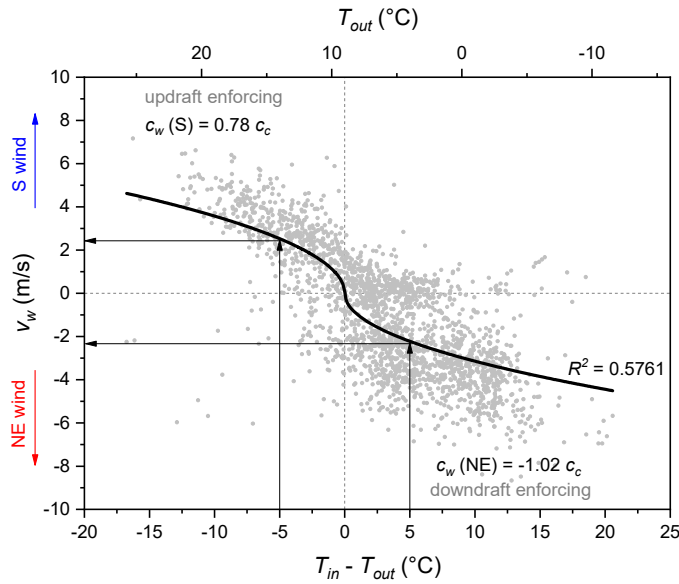
484

485   Fig. 15. Relationship between wind velocity and temperature difference under the condition when cave ventilation stops or is close to
486   zero |v| < 0.1 m/s. The square-root relationship is indicated by the black curve. Several threshold values of this effect can be read
487   (black arrows), which are explained in the text.

488   Using the previous estimates, we can now calculate the relative contribution of wind pressure for

489   NE and S winds (Fig. 16). All observations with outside wind in the given interval (-10°C < T_{out} <

490   30°C) were used and Δp_c and Δp_w were calculated from Eq. 1 and Eq. 4. Point kriging with an

491   interval of 0.4 K and 0.4 m/s was used. As an example, the isoline with value 0.5 indicates all

492   combinations of T_{out} and v_w where wind-driven effect and chimney effect are equal.
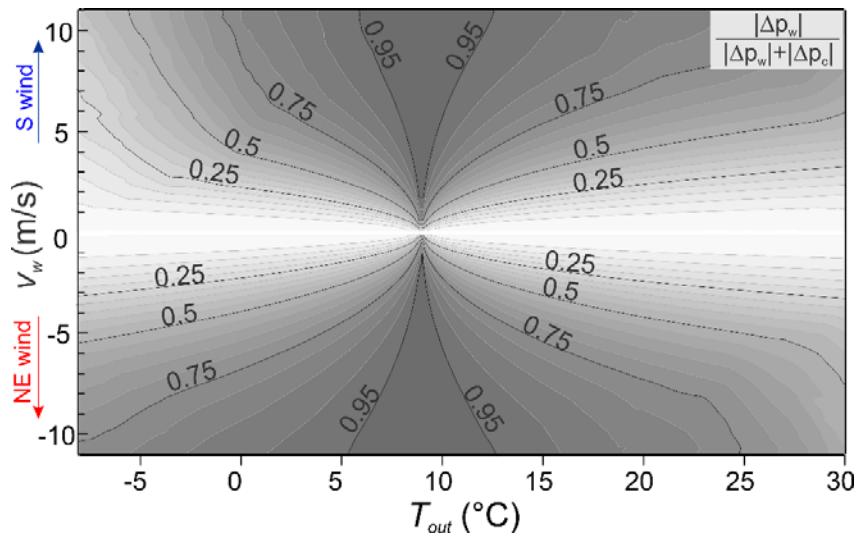
Fig. 16. Contour plot of the relative contribution of wind pressure to total driving pressure (from 0.25 to 0.95 in 0.05 intervals) for different outside temperatures and wind velocities. As expected, the contribution increases with wind velocity and decreases for positive or negative outside temperature extremes.

Fig. 15 can also be used to find some useful thresholds for the wind-driven effect, regardless of pronounced scatter. Ideally, the relationship described by the black curve (with the conditions of the second approach to calculating Δp_w) gives an estimate of the minimum wind speed necessary to counteract the theoretical driving force of the chimney flow. For example, the black arrows show that a downdraft caused by the chimney flow at $\Delta T = -5°C$ could be stopped by as little as 2.5 m/s S wind, or that the updraft at $\Delta T = 5°C$ could be stopped by 2.2 m/s NE wind. At $|\Delta T| = 10°C$ this increases to 3.6 m/s for the S wind, or 3.1 m/s for the NE wind. Similar values are obtained from Fig. 16 using the isoline 0.5. Such wind speeds are quite common in Postojna, as shown by the frequency distribution curves in Fig. 17a, where about 60% of the time the wind will be higher than 2 m/s and more than 20% of the time higher than 4 m/s. In general, we can expect the wind-driven effect to be active throughout the year in Postojna Cave. As for the range of temperature differences, $|\Delta T|$ less than 5°C will occur ~40% of the time and less than 10°C ~70% of the time (Fig. 17b).
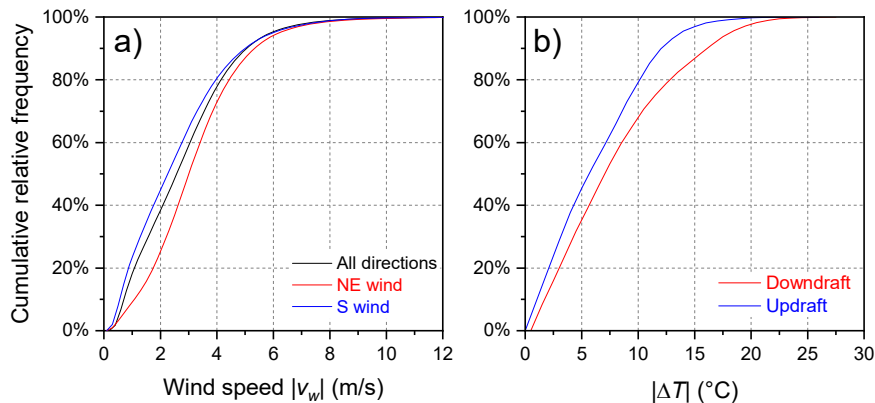
Fig. 17. Cumulative frequency distribution for wind speeds in Postojna (a) and temperature difference ($T_{in} - T_{out}$) for Postojna Cave (b). Both NE winds and downdraft are favored over other wind/airflow direction, suggesting a larger wind-driven effect in winter than in summer.

In comparing the seasonal differences in the wind-driven effect, the winter period is windier than the summer period (as shown in Fig. 7). The NE winds are strongest in January, February, and March, when one might expect the greatest interference of the typical winter updraft. An extreme example was February 2018, when the NE winds restricted ventilation for most of the month, leading to an unexpected increase in cave pCO$_2$ (Kukuljan et al., 2021). On the other hand, S winds are weakest in July, August, and September, and therefore we can expect the least inference of typical summer downdraft. These could be the reasons for a rougher and more variable signal of the cave airflow for the winter period than for the summer (Fig. 5), and consequently for a larger scatter when comparing the airflow with ΔT in Fig. 11. Overall, the frequency distribution in Fig. 17a and b also shows how NE winds are preferred over other directions and how updraft is less frequent than downdraft, again indicating a stronger wind-driven effect in cooler periods.

CONCLUSIONS

Airflow in caves can be driven by different mechanisms. In this study, we show how near-surface pressure differences induced by outside winds interact with the chimney effect. The wind pressure between two cave entrances or air inlets or outlets depends on the relationship between the surface topography and the position of the air inlets or outlets, as well as the strength and direction of the wind. Outside winds can increase, decrease, or completely reverse airflow driven solely by the

531 chimney effect. We used a CFD model to quantify the surface pressure field over the Postojna Cave

532 system for winds of varying strength and direction. Despite the complexity of the cave system, the

533 results show good agreement with pressure differences calculated from the data and from a simple

534 empirical estimate of the chimney flow pressure. Wind pressure may become a dominant driving

535 mechanism when cave systems have entrances at similar heights, such as in caves formed in karst

536 plateaus. By affecting normal cave ventilation, winds can determine the dynamics and composition

537 of air in the karst vadose zone and associated processes, including dissolution and precipitation of

538 calcite. The analysis of outside winds should therefore be a necessary component of microclimatic

539 studies in caves.

554   **AUTHORSHIP STATEMENT**

555   LK performed the data analyzes, produced most of the figures and, wrote the initial draft. FG

556 initiated the study, designed the measurement network (with B. Grašič and P. Mlakar), analyzed

557 and compiled the results of the CFD model. LK and FG interpreted the data. MDC added critical

558 input and suggestions for additions and improvements, and proofread the manuscript. All authors

559 read and approved the final version of the manuscript.

560   **REFERENCES**

561 Allard, F., Ghiaus, C., 2006. Natural ventilation in the Urban environment, in: Building Ventilation: The State of the

562   Art. pp. 1–37.

563 ARSO, 2021. Ministry of the environment and spatial planning, Slovenian Environmental Agency. URL

564   http://meteo.arso.gov.si/met/en/ [accessed May 6, 2021].

565 ARSO, 2020. Ministry of the environment and spatial planning, Slovenian Environmental Agency. URL

566   http://gis.arso.gov.si/evode/profile.aspx?id=atlas_voda_Lidar@Arso [accessed July 2, 2020].

567 Badino, G., 2010. Underground meteorology - "What's the weather underground?" Acta Carsologica 39, 427–448.

568 Badino, G., Chignola, R., 2019. Fluctuations of atmospheric pressure and the sound of underground Karst systems:

569   The Antro del Corchia Case (Apuane Alps, Italy). Front. Earth Sci. 7, 1–6.

570   https://doi.org/10.3389/feart.2019.00147

571 Borsato, A., Frisia, S., Miorandi, R., 2015. Carbon dioxide concentration in temperate climate caves and parent soils

572   over an altitudinal gradient and its influence on speleothem growth and fabrics. Earth Surf. Process. Landforms

573   40, 1158–1170. https://doi.org/10.1002/esp.3706

574 Cigna, A., 1968. An analytical study of air circulation in caves. Int. J. Speleol. 3, 41–54. https://doi.org/10.5038/1827-

575   806x.3.1.3

576 Conn, H.W., 1966. Barometric wind in Wind and Jewel Caves, South Dakota. Natl. Speleol. Soc. Bull. 28, 55–69.

577 Covington, M.D., Knierim, K.J., Young, H.A., Rodriguez, J., Gnoza, H.G., 2021. The impact of ventilation patterns

578   on calcite dissolution rates within karst conduits. J. Hydrol. 593, 125824.

579   https://doi.org/10.1016/j.jhydrol.2020.125824

580 Covington, M.D., Perne, M., 2015. Consider a cylindrical cave: A physicist's view of cave and karst science. Acta

581   Carsologica 44, 363–380. https://doi.org/10.3986/ac.v44i3.1925

582 Fairchild, I.J., Baker, A., 2012. Speleothem Science: From Process to Past Environments. A John Wiley & Sons, Ltd.

583   https://doi.org/10.1002/9781444361094

584 Gabrovšek, F., Grašic, B., Božnar, M.Z., Mlakar, P., Udén, M., Davies, E., 2014. Karst show caves - How DTN

585   technology as used in space assists automatic environmental monitoring and tourist protection - Experiment in

586   Postojna Cave. Nat. Hazards Earth Syst. Sci. 14, 443–457. https://doi.org/10.5194/nhess-14-443-2014

Gregorič, A., Vaupotič, J., Gabrovšek, F., 2013. Reasons for large fluctuation of radon and CO2 levels in a dead-end passage of a karst cave (Postojna Cave, Slovenia). Nat. Hazards Earth Syst. Sci. 13, 287–297. https://doi.org/10.5194/nhess-13-287-2013

Grisogono, B., Belušić, D., 2009. A review of recent advances in understanding the meso- and microscale properties of the severe Bora wind. Tellus, Ser. A Dyn. Meteorol. Oceanogr. 61 A, 1–16. https://doi.org/10.1111/j.1600-0870.2008.00369.x

James, E.W., Banner, J.L., Hardt, B., 2015. A global model for cave ventilation and seasonal bias in speleothem paleoclimate records. Geochemistry, Geophys. Geosystems 16, 1044–1051. https://doi.org/10.1002/2014GC005658

Kašing, M., Lenart, J., 2020. Cave airflow mechanism of a crevice-type cave: A case study from Czechia. Int. J. Speleol. 49, 55–67. https://doi.org/10.5038/1827-806X.49.1.2285

Kowalczk, A.J., Froelich, P.N., 2010. Cave air ventilation and CO2 outgassing by radon-222 modeling: How fast do caves breathe? Earth Planet. Sci. Lett. 289, 209–219. https://doi.org/10.1016/j.epsl.2009.11.010

Kozjek, K., Dolinar, M., Skok, G., 2017. Objective climate classification of Slovenia. Int. J. Climatol. 37, 848–860. https://doi.org/10.1002/joc.5042

Kukuljan, L., Gabrovšek, F., Covington, M.D., Johnston, V.E., 2021. CO2 dynamics and heterogeneity in a cave atmosphere: Role of ventilation patterns and airflow pathways. Theor. Appl. Climatol. (in press).

Lopes, A.M.G., 2003. Windstation - A software for the simulation of atmospheric flows over complex topography. Environ. Model. Softw. 18, 81–96. https://doi.org/10.1016/S1364-8152(02)00024-5

Luetscher, M., Lismonde, B., Jeannin, P.Y., 2008. Heat exchanges in the heterothermic zone of a karst system: Monlesi cave, Swiss Jura Mountains. J. Geophys. Res. Earth Surf. 113, 1–13. https://doi.org/10.1029/2007JF000892

Mattey, D.P., Atkinson, T.C., Hoffmann, D.L., Boyd, M., Ainsworth, M., Durrell, R., Latin, J.-P., 2021. External controls on CO2 in Gibraltar cave air and ground air: implications for interpretation of δ13C in speleothems. Sci. Total Environ. 146096. https://doi.org/10.1016/j.scitotenv.2021.146096

Mlakar, P., Grašič, B., Božnar, M.Z., Popović, D., Gabrovšek, F., 2020. Information system for scientific study of the micrometeorology of karst caves - Case of Postojnska jama Cave, Slovenia 49, 297–310. https://doi.org/10.3986/ac.v49i2-3.7540

NOAA/ESRL, 2021. Global Greenhouse Gas Reference Network. Global Monthly Mean CO2. URL https://www.esrl.noaa.gov/gmd/ccgg/trends/global.html [accessed May 13, 2020].

616 Noronha, A.L., Hardt, B.F., Banner, J.L., Jenson, J.W., Partin, J.W., James, E.W., Lander, M.A., Bautista, K.K., 2017.
617   Trade winds drive pronounced seasonality in carbonate chemistry in a tropical Western Pacific island cave—
618   Implications for speleothem paleoclimatology. Geochemistry, Geophys. Geosystems 18, 384–399.
619   https://doi.org/10.1002/2016GC006644

620 Pflitsch, A., Piasecki, J., Wiles, M., Horrocks, R., Ringeis, J., 2010. Dynamic climatologic processes of barometric
621   cave systems using the example of Jewel Cave and Wind Cave in South Dakota, USA. Acta Carsologica 39,
622   449–462. https://doi.org/10.3986/ac.v39i3.75

623 Prelovšek, M., Šebela, S., Turk, J., 2018. Carbon dioxide in Postojna Cave (Slovenia): spatial distribution, seasonal
624   dynamics and evaluation of plausible sources and sinks. Environ. Earth Sci. 77. https://doi.org/10.1007/s12665-
625   018-7459-6

626 Rakovec, J., Žagar, M., Bertalanic, R., Cedilnik, J., Gregoric, G., Skok, G., Žagar, N., 2009. Vetrovnost v Sloveniji
627   [Wind conditions in Slovenia]. Založba ZRC, ZRC SAZU.

628 Riechelmann, S., Breitenbach, S.F.M., Schröder-Ritzrau, A., Mangini, A., Immenhauser, A., 2019. Ventilation and
629   cave air PCO2 in the bunker-EMST cave system (NW Germany): Implications for speleothem proxy data. J.
630   Cave Karst Stud. 81, 98–112. https://doi.org/10.4311/2018ES0110

631 Šebela, S., 2019. Postojna—Planina Cave System, Slovenia, in: White, W.B., Culver, D.C., Pipan, T.B.T.-E. of C.
632   (Third E. (Eds.), Encyclopedia of Caves. Academic Press, pp. 812–821.
633   https://doi.org/https://doi.org/10.1016/B978-0-12-814124-3.00098-4

634 Šebela, S., 2010. Accesses from the surface to the Postojna Cave system. Ann. Ser. Hist. Nat. 20, 55–64.

635 Šebela, S., Turk, J., 2011. Local characteristics of Postojna Cave climate, air temperature, and pressure monitoring.
636   Theor. Appl. Climatol. 105, 371–386. https://doi.org/10.1007/s00704-011-0397-9

637 Yang, T., Clements-Croome, D., 2012. Natural Ventilation in Built Environment. pp. 6865–6896.
638   https://doi.org/10.1007/978-1-4419-0851-3_488

639 Zheng, X., Shi, Z., Xuan, Z., Qian, H., 2018. Natural Ventilation, in: Wang, R., Zhai, X. (Eds.), Handbook of Energy
640   Systems in Green Buildings. Springer Berlin Heidelberg, Berlin, Heidelberg, pp. 1227–1270.
641   https://doi.org/10.1007/978-3-662-49120-1_8

642